Article:
Vardakis, JC, Guo, L, Peach, TW et al. (8 more authors) (2019) Fluid–structure interaction for highly complex, statistically defined, biological media: Homogenisation and a 3D multi-compartmental poroelastic model for brain biomechanics. Journal of Fluids and Structures, 91. 102641. ISSN 0889-9746

https://doi.org/10.1016/j.jfluidstructs.2019.04.008

Fluid-Structure Interaction for Highly Complex, Statistically Defined, Biological Media: Homogenisation and a 3D Multi-Compartmental Poroelastic Model for Brain Biomechanics

John C. VARDAKIS[1], Liwei GUO[1], Thomas W. PEACH[1], Toni LASSILA[3], Micaela MITOLO[5], Dean CHOU[2], Zeike A. TAYLOR[4], Susheel VARMA[7], Annalena VENNERI[6], Alejandro F. FRANGI[3] & Yiannis VENTIKOS[1]

*[1]Department of Mechanical Engineering, University College London, Torrington Place, London, WC1E 7JE, UK, *email: y.ventikos@ucl.ac.uk*

[2]Department of Mechanical Engineering, National Central University, Taoyuan County, Taiwan

[3]Centre for Computational Imaging & Simulation Technologies in Biomedicine (CISTIB), School of Computing, University of Leeds, UK

[4]Centre for Computational Imaging & Simulation Technologies in Biomedicine (CISTIB), School of Mechanical Engineering, University of Leeds, UK

[5]Functional MR Unit, Policlinico S. Orsola e Malpighi, Department of Biomedical and NeuroMotor Sciences (DiBiNeM), Bologna, Italy.

[6]Department of Neuroscience, Medical School, University of Sheffield, UK.

[7]The European Bioinformatics Institute (EMBL-EBI), Wellcome Genome Campus, Cambridge, UK

Abstract

Numerous problems of relevance in physiology and biomechanics have at their core the presence of a deformable solid matrix which experiences flow-induced strain. Often, this fluid-structure interaction is directed the opposite way, i.e. it is solid deformation that creates flow, which the heart being the most prominent example. In many cases this interaction of fluid and solid is genuinely two-way and strongly coupled, with solid deformation inducing flow and fluid pressure deforming the solid. Although a fluid-structure interaction problem, numerous cases in biomechanics are not tractable via the traditional FSI methodologies: in the internal flows that are of interest to use, the number and range of fluid passage is so vast that the direct approach of a deterministically defined boundary between fluid and solid is impossible to apply. In these cases, homogenisation and statistical treatment of the material-fluid system is possibly the only way forward. Such homogenization, quite common to flow-only systems through porous media considerations, is also possible for fluid-structure interaction systems, where the loading is effectively internal to the material. A prominent technique of this type is that of poroelasticity. In this paper, we discuss a class of poroelastic theory techniques that allow for the co-existence of a multitude of – always statistically treated –channels and passages of widely different properties: termed multiple-network poroelasticity (or multicompartmental poroelasticity), this paradigm is particularly suitable for the study of living tissue, that is invariably permeated – perfused – by fluids, often different in nature and across a wide range of scales. Multicompartmental poroelasticity is capable of accounting for a full two-way coupling between the fluids and the solid matrix and allows us to track transport of a multitude of substances together with the deformation of the solid material that this transport gives rise to or is caused by, or both. For the purposes of demonstration, we utilise a complex and physiologically very important system, the human brain, to exemplify the qualities and efficacy of this methodology. The methodology we present has been implemented through the Finite Element Method, in a general manner, allowing for the co-existence of an arbitrary number of compartments. For the applications used in this paper to exemplify the method, a four-compartment implementation is used. A unified pipeline is used on a cohort of 35 subjects to provide statistically meaningful insight into the underlying mechanisms of the neurovascular unit (NVU) in the hippocampus, and to ascertain whether physical activity would have an influence in the both swelling and drainage by taking into account both the scaled strain field and the proportion of perfused blood injected into the brain tissue. A key result garnered from his study is the statistically significant differences in right hemisphere hippocampal NVU swelling between CHC males and MCI females during high and low activity states.

Key words: Multiple-Network Poroelastic Theory, Finite Element Method, Brain Biomechanics, Dementia, Neurovascular Unit

1. INTRODUCTION

Fluid-Structure Interaction (FSI) methods allow for the coupling of solid and fluid mechanics phenomena and enable the study of processes that involve the exchange of loads between the two (or more media), the fluid and the solid [1]. An example of an internal flow where such interactions are at play is shown in Figure 1: In the first part of this figure, Figure 1a, a deformable solid is shown, which is permeated by a series of channels, or arbitrary shape with non-trivial interconnections. In this case, traditional FSI methods can capture the flow field in the channels/passages and the deformation field of the solid matrix, Figure 1b, since it is straightforward and computationally feasible to mesh the two domains (in a wide variety of ways) and solve the coupled problem.

The challenge necessitating a different viewpoint is illustrated in Figure 1c which of course can be further complicated almost ad infinitum, to the limit of real biological materials, Figure 1d: for the latter figure, it becomes extremely difficult, and in most cases intractable computationally, to discretize the multitude of fluid channels, as well as the fine solid ligaments and strands that define them; it is clear that an alternative is needed. An approach that is often used, originally in geotechnical engineering and groundwater studies and as of recently in increasing frequency within the field of biomedical engineering, is that of poroelasticity.

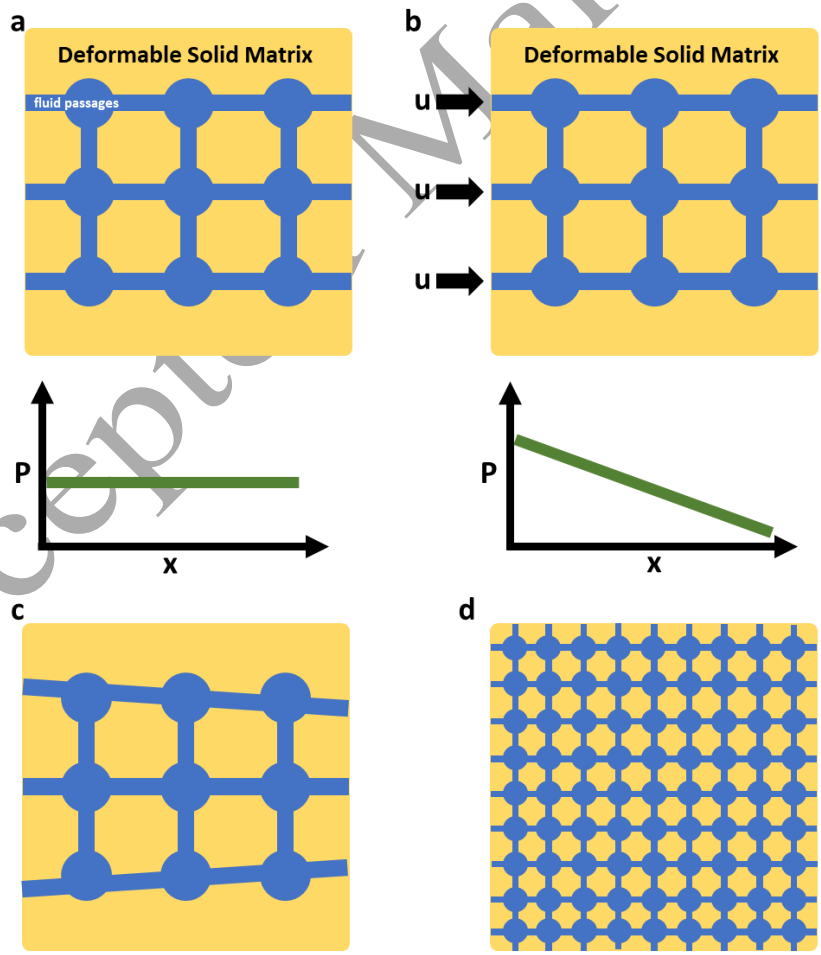

Figure 1: a) Porous matrix of a deformable solid, when no flow is present, at equilibrium b) when flow is present, a pressure field develops which loads and deforms the solid matrix, c) direct FSI through detailed deterministic meshing captures flow and deformation fields, d) highly complex network of fluid passages render direct FSI methods through discretisation of the exact deterministic interface and passages computationally impractical or impossible.

1.1 POROELASTICITY

Poroelastic systems describe fluid flow through a porous medium coupled with deformation of the solid matrix. The fundamental poroelastic equations consist of conservation of mass and momentum equations, which are derived at the macroscopic scale [2-4], effectively assuming a statistical representation of the fluid passages and the fluid/solid interface; a homogenisation approach. Building on the principles of linear elasticity, the conservation of momentum in a poroelastic system also includes a fluid pressure term (as a measure of the effect of the fluid in the medium). It is also worth noting that deformation of the medium is usually much slower than the flow rate, and therefore inertial terms are ignored in the formulation, ultimately incorporating a quasistatic assumption. The momentum equation is derived by considering the total stress, $\tilde{\boldsymbol{\sigma}}$, and a body force, $\mathbf{f}$, leading to:

$$-\nabla \cdot \tilde{\boldsymbol{\sigma}} = \mathbf{f} \tag{1}$$

The total stress (see Table 1) tensor accounts for the fluid pressure in addition to the material stress tensor (or effective stress) as derived from linear elasticity.

The conservation of mass is derived from the fluid content of the medium, $\boldsymbol{\zeta}$, the volumetric fluid flux, $\mathbf{v}_f$, and any additional volumetric fluid source/sink terms. The final form of this conservation equation is of the form:

$$\frac{\partial \zeta}{\partial t} = -\nabla \cdot \mathbf{v}_f + h \tag{2}$$

The model is closed by assuming the constitutive relationships summarised in Table 1 [5]:

Table 1: Summary of constitutive relations

Relation	**Description**
$\tilde{\boldsymbol{\sigma}}_{ij}(\mathbf{u}, p) = \boldsymbol{\sigma}_{ij}(\mathbf{u}) - \alpha\delta_{ij}\, p$	Total stress
$\boldsymbol{\sigma}_{ij}(\mathbf{u}) = \lambda\delta_{ij}\varepsilon_{kk}(\mathbf{u}) + 2\mu\varepsilon_{ij}(\mathbf{u})$	Effective stress
$\boldsymbol{\zeta} = c_j\, p + \alpha\nabla \cdot \mathbf{u}$	Fluid content
$\mathbf{v_f} = -\mathbf{K}(\nabla p - \rho_f \mathbf{g})$	Volumetric fluid flux (Darcy's Law)

These relationships relate the total stress, volumetric fluid flux and fluid content to the primary variables of the two-field formulation, namely the solid matrix displacement (**u**) and scalar pore pressure (p). For the fluid content relationship, the $c_j\, p$ term represents the amount of fluid that can be injected into a fixed material volume, whilst the $\alpha\nabla \cdot \mathbf{u}$ term is a measure of the amount of fluid that can be squeezed out of the same volume.

1.2 GOVERNING EQUATIONS AND MODELLING

Building on the principles of poroelasticity, the standard mathematical model for diffusive flow in an elastic porous medium is the diffusion-deformation model of poroelasticity proposed by Biot [2]. This is based on the coupling between the pore-fluid potential and the solid-stress fields. An extension of Barenblatt's double-diffusion approach [6] and Biot's diffusion-deformation theory leads to the

Barenblatt-Biot poroelastic model representing multiple-network diffusion in elastic porous media. This model takes the following form:

$$-\nabla\cdot\left(\mathbb{C}:\varepsilon(u)\right)+\sum_{j=1}^{A}\alpha_j\nabla p_j = f,$$

$$c_j\dot{p}_j+\alpha_j\nabla\cdot\dot{u}-\nabla\cdot\left(K_j\nabla p_j\right)+\sum_{i=1}^{A}\xi_{j\to i}\left(p_j-p_i\right)=h \qquad \text{(3a-b)}$$

In the above formulation, for a given number of networks, $A\in\mathbb{N}$, the displacement of the solid skeleton is given by $u=u(x,t)$, whilst the fluid potentials for each respective compartment is given by $p_j=p_j(x,t)$, where $1\le j\le A$ for $x\in\Omega\subset\mathbb{R}^d\,(d=1,2,3)$, and $t\in[0,T]$. The Biot-Willis coefficient (which traditionally couples the momentum and mass conservation equations, see Table 1), $\alpha_j\in(0,1]$, for each compartment satisfies $\phi\le\Sigma\alpha_j\le 1$, where ϕ is the total porosity., $c_j\ge 0$ is the constrained specific storage coefficient, K_j is the symmetric and uniformly positive definite hydraulic permeability tensor defined by $K_j=\kappa_j\left(\mu_j\right)^{-1}>0$ (the ratio of the compartmental permeability tensor, κ, to fluid viscosity), $\xi_{j\to i}$ is the intercompartmental transfer coefficient, $f=f(x,t)$ represents a body force and $h=h_j(x,t)$ represent any additional compartment specific source/sink terms. In this manuscript, $\varepsilon(u)$ denotes the small-strain tensor derived from the symmetric part of the of the gradient of the solid matrix displacement u:

$$\varepsilon(u):=\frac{1}{2}\left(\nabla u+(\nabla u)^T\right) \qquad (4)$$

The elastic stiffness tensor, $\mathbb{C}$, defines a stress tensor σ using Hooke's Law:

$$\sigma:=\mathbb{C}\varepsilon(u) \qquad (5)$$

We assume an isotropic and homogeneous linear elastic medium with elasticity tensor, $\mathbb{C}$, defined by the identity:

$$\mathbb{C}:\varepsilon(u)=2\mu\varepsilon(u)+\lambda(\nabla\cdot u)\mathbf{I} \qquad (6)$$

where **I** is the identity tensor, and μ and λ are the Lamé moduli.

It is useful at this stage to describe a field of application of the above class of methodologies, namely biomechanics and in particular the biomechanics of brain diseases. Brain disorders such as developmental and neurodegenerative diseases represent an enormous healthcare burden, not only in terms of human distress, but also economic cost (in Europe, this figure approaches 1 trillion euros [7]). Cognition is a group of mental processes which include memory, attention, learning, decision making, problem solving, language processing and executive functions. Dementia is classified as a progressive cognitive disorder which primarily affects memory, but additional symptoms also include aphasia, apraxia, agnosia, and lifestyle impairments [8]. The most common form of dementia is Alzheimer′s disease (AD), and the major risk factor for its development is increasing age [9], in addition to other known factors, such as hypertension and hypotension, heart failure, low levels of physical activity and of education, obesity, and genetic factors [8, 10-13].

Interestingly, there is a growing body of evidence that suggests a close association between cardiovascular risk and cognitive impairment and dementia [14]. Furthermore, it is also postulated that cardiovascular risks are associated with modifiable risk factors (such as physical inactivity, depression, hypertension, and smoking), so it may be possible to improve brain health and to delay the onset of dementia in later life (see Figure 2a). Delaying the onset of AD by just 1 year would lead to an estimated 9 million fewer cases by 2050 [15].

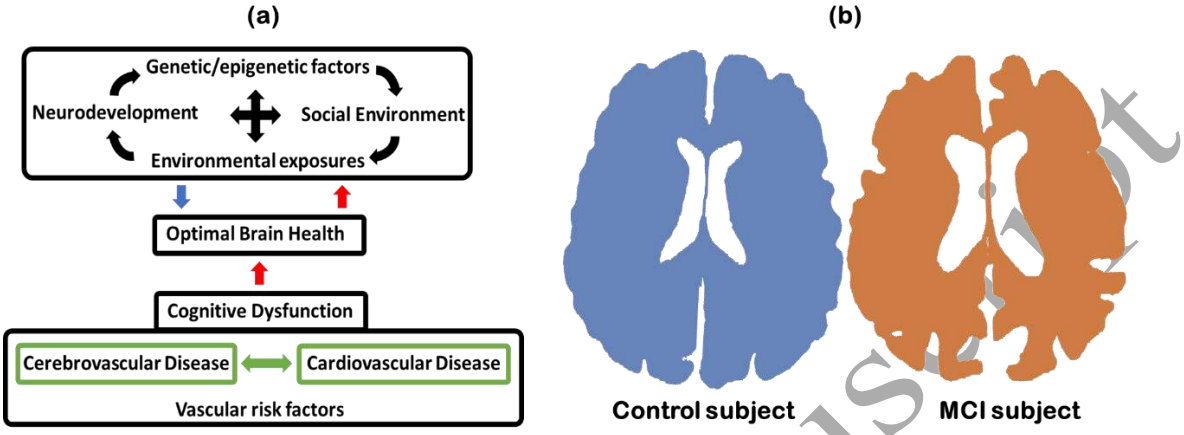

Figure 2: (a) Determinants of optimal brain health. The blue arrow denotes factors that can promote optimal brain health, whilst the red arrows indicate factors that hinder brain health. Neurodevelopmental, genetic and environmental factors can therefore promote or hinder brain health. (b) An example of cerebroventricular dilatation from the cohort used in this study. The horizontal section of a cognitively healthy control subject (female, 68 years old) can be seen to possess smaller cerebral ventricles than the mild cognitively impaired subject (female, 62 years old). Similarly enlarged cerebroventricular representations exist for hydrocephalic patients, as ventriculomegaly is an overlapping characteristic of this disorder.

1.3 HYDROCEPHALUS

Although a precise definition is controversial, hydrocephalus (HCP) can be succinctly described as the abnormal accumulation (imbalance between production and circulation) of cerebrospinal fluid CSF within the brain [16-20]. This balance of CSF production and reabsorption normally allows the maintenance of the CSF pressure to lie within a tight range. HCP is classified with regards to whether the point of CSF obstruction or discrete lesion lies within the ventricular system (obstructive) and obstructs the flow before it enters the subarachnoid space (SAS) [21], or not (communicating). There is currently no definitive cure for this disorder. Dilatation of the cerebroventricular system (see Figure 2b) can lead to loss of brain cells that ultimately results in a variety of neurological symptoms (such as AD described in the next section), stroke, and sometimes even death due to pressure applied on the brain parenchyma [22].

1.4 ALZHEIMER'S DISEASE, MILD COGNITIVE IMPAIRMENT AND THE HIPPOCAMPUS

AD can be deemed as a heterogeneous mixture of multiple age-related neurodegenerative factors and vascular related pathologies. The hallmark pathological features of the disease are the extracellular deposition of amyloid-β (Aβ) peptide into parenchymal senile plaques or within the walls of arteries and capillaries, in addition to the aggregation of hyperphosphorylated tau into intracellular neurofibrillary tangles and neuropil threads [23-24]. Evidence also suggests that AD may be a vascular disorder [25-26], caused by impaired cerebral perfusion (characterized by reduction in both total and regional CBF [27]) [26, 28], which is observable at the early stages of the disease [29-31]. This reduction in perfusion can compromise the oxygenation of neurons, negatively affect the synthesis of proteins required for memory and learning and subsequently lead to neuronal dysfunction or death [32-33]. Ultimately, the final consideration that needs to be made is the clearance of Aβ at the level of the blood–brain barrier (BBB). The BBB forms an important part of the neurovascular unit (NVU), a

functional cellular structure that allows for the highly efficient regulation of CBF. The BBB consists of endothelial cells connected by tight junctions and a thick basement membrane which is supported by astrocytic end feet (see Figure 3). Communication between the cells of the NVU is required to enable efficient clearing of Aβ to prevent it from accumulating in the form of plaques [34]. Breakdown of the BBB ultimately results in the impaired clearance of Aβ, leading to amyloid accumulation in the brain parenchyma and in and around capillaries. The latter process is known as cerebral amyloid angiopathy (CAA), and it is defined as a major pathological insult to the NVU [35]. CAA is associated with cognitive impairment [36], is accelerated by hypoperfusion and is present in over 80% of patients with AD [37].

One of the overarching foci of neuropsychology [38] since the turn of this century has been to better understand the prodromal stages of AD. During this early stage, AD may present itself as mild cognitive impairment (MCI), an intermediate state between normal ageing and dementia. Traditionally, MCI has been defined as a condition whereby an individual experiences memory loss to a greater extent than that expected for that age, but does not meet the criteria for dementia [38].

The hippocampus is small structure in the brain, and it plays an important role in spatial and episodic memory. It is the region of the brain that tends to show the most rapid loss of tissue earliest in the disease course. Reduced hippocampal volume results in an amnestic syndrome, a core feature of Alzheimer's disease [39].

1.5 MODELLING ALZHEIMER'S DISEASE USING POROELASTICITY

In the literature, several works have utilised a poroelastic approach in modelling parenchymal tissue within the realm of hydrocephalus and oedema formation in the small intestine [16, 20, 40, 52, 61, 70-80]. The poroelastic modelling of parenchymal tissue for the purpose of investigating Alzheimer's Disease yields a narrower selection of relevant work [40, 80]. Recently, Aldea and colleagues [80] utilise poroelastic theory in a multiscale model of arteries in order to test the hypothesis that cerebrovascular smooth muscle cells drive intramural periarterial drainage. Guo and colleagues [40] introduce a pipeline that intertwines a general 3D multiple-network poroelastic model of perfused parenchymal tissue, an image-based modelling pipeline and a detailed subject-specific boundary condition model that can be used to model the influence of lifestyle and environmental factors in obtaining novel biomarkers during the MCI stage of AD.

1.6 OUTLINE OF THE ARTICLE

This work uses a novel consolidated pipeline that integrates three important components: a three-dimensional multiple-network poroelastic theory (MPET)-based model of perfused cerebral parenchyma; an accurate, fully automated image-based model personalization workflow [40]; and a subject-specific boundary condition model that is targets the driving compartment of the MPET model. Specifically, MPET is allows for the detailed investigation of spatio-temporal transport of fluid between the cerebral blood (arteries, capillaries and veins), cerebrospinal and interstitial fluid (CSF/ISF) and brain parenchyma across multiple scales. This pipeline is used on a cohort of subjects (both cognitively healthy controls and mild cognitively impaired subjects stratified with respect to gender) in order to assess two novel biomarkers (swelling and drainage which is derived from the fluid content of the capillary compartment of the four-network MPET model described in §2) during the early stages of AD. This is done by providing insight into the underlying mechanisms of the neurovascular unit in the hippocampus for both controls and cognitively impaired subjects during two states of activity (high and low) within a 24-hour period. The essential breakdown of the methodology behind the full implementation scheme follows in §2, which highlights the consolidated pipeline embedded within the VPH-DARE@IT research platform, the prospective data collection programme used to extract the subject-specific data (including boundary conditions) for the 35 subjects used in this study, and an outline of the statistical analyses used to analyse the MPET results (swelling and

drainage). The results are given in §3, where two MPET simulations are presented (based on one control and one MCI subject) in order to depict the nature of the solution fields that are obtainable at the level of the parenchyma. Subsequently, a three-way mixed ANOVA was conducted in to understand the effects of gender, cognitive status and activity on blood flow rate in the left and right ICA and VA (as the blood flow rate was a key driver in the MPET model), followed by a Kruskal-Wallis H-test (to determine if there were differences in NVU swelling and drainage in the hippocampus between the groups considered, during two levels of activity) and Wilcoxon signed-rank test (to determine whether there was no statistically significant median decrease in NVU swelling and drainage in the hippocampus when subjects lowered their activity level). The results are discussed in §4, along with limitations and perspectives for future work. The conclusions to the paper are given in §5.

2. METHODOLOGY

Modelling the transport of fluid within the brain, in a personalised manner and from first principles, is essential to help decipher some of the underlying mechanisms that are currently being investigated regarding diseases of the cerebral environment, such as hydrocephalus and AD. An MPET model for perfused parenchymal tissue is coupled with an automated image-based model personalization workflow [40], and a subject-specific blood flow variability model. The consolidated pipeline will then be used on a small cohort of 35 subjects and used to provide insight into the underlying mechanisms of the NVU in the hippocampus.

In the previous section, we discussed the basic governing equations of poroelasticity and how they can be cast for multiple compartments. In this section we shall briefly present a formulation where four compartments are used, and we shall describe a computational framework where these equations are solved using the Finite Element Method.

2.1 THREE-DIMENSIONAL MPET MODEL FOR THE CEREBRAL ENVIRONMENT

In this paper, the MPET model was used to conduct mechanistic modelling of fluid transport through the brain parenchyma. Biologically, the solid matrix represents brain parenchyma, and the communicating fluid phases considered are: an arterial network (a), an arteriole/capillary network (c), a CSF/ISF network (e) and a venous network (v) (see Figure 3). This model allows for the simultaneous solutions of continuity and momentum conservation equations, in four interconnected fluid compartments, within a deformable solid matrix (the parenchymal tissue).

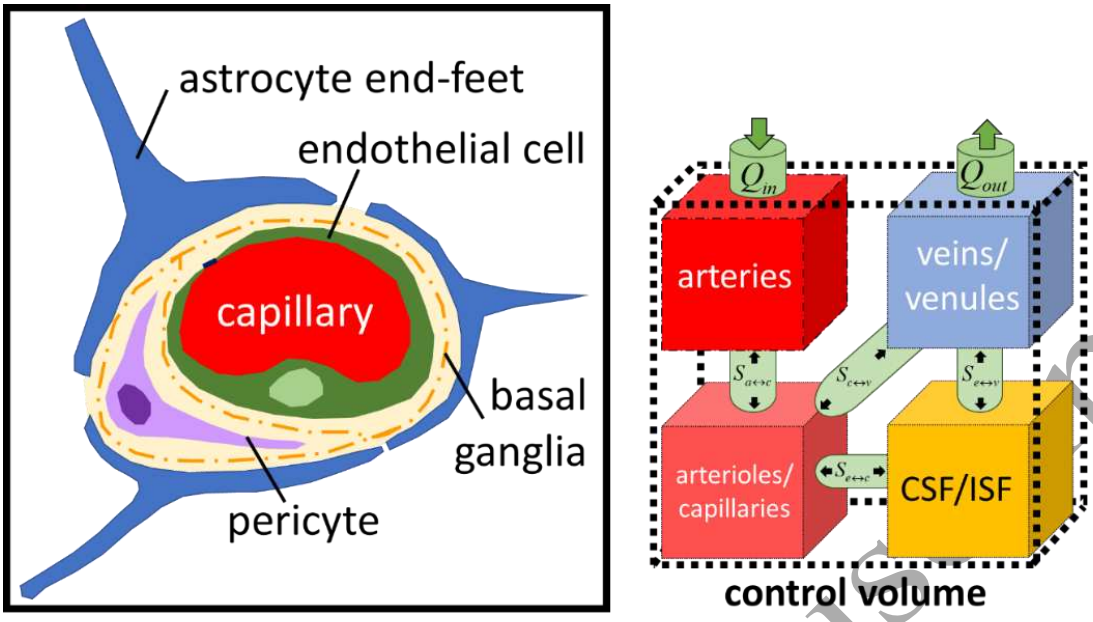

Figure 2. (Left) A schematic representation of the Neurovascular unit (NVU) (Right) The four-compartment MPET model reflect the key fluid transport mechanisms in the brain tissue. Flow is prohibited between the CSF/ISF and the arterial network, whilst directional transfer exists between (a) and (c), (c) and (v), (c) and (e) and finally (e) and (v).

The MPET model uses the parenchymal tissue displacement (**u**), and the pore pressures of the four fluid compartments (p_a, p_c, p_e, p_v) as the primitive variables in the governing equations, which are given below:

$$
\begin{aligned}
&G\nabla^2\mathbf{u} + (G+\lambda)\nabla\varepsilon = \alpha_a\nabla p_a + \alpha_c\nabla p_c + \alpha_e\nabla p_e + \alpha_v\nabla p_v \\
&c_a\dot{p}_a + \alpha_a\nabla\cdot\dot{\mathbf{u}} - \nabla\cdot(\mathbf{K_a}\nabla p_a) = S_{c\to a} \\
&c_c\dot{p}_c + \alpha_c\nabla\cdot\dot{\mathbf{u}} - \nabla\cdot(\mathbf{K_c}\nabla p_c) = S_{a\to c} + S_{e\to c} + S_{v\to c} \qquad (7a\text{-}e) \\
&c_e\dot{p}_e + \alpha_e\nabla\cdot\dot{\mathbf{u}} - \nabla\cdot(\mathbf{K_e}\nabla p_e) = S_{c\to e} + S_{v\to e} \\
&c_v\dot{p}_v + \alpha_v\nabla\cdot\dot{\mathbf{u}} - \nabla\cdot(\mathbf{K_v}\nabla p_v) = S_{c\to v} + S_{e\to v}
\end{aligned}
$$

The S terms in Equation 7b-e define spatially varying source ($S_{ij} > 0$) or sink ($S_{ij} < 0$) densities (rate of fluid transfer between networks). More details can be found in Guo et al. [40]. As described in §1, **K** is the hydraulic permeability tensor for each fluid compartment. It is defined as $\boldsymbol{\kappa}(\mu^{-1})$, where $\boldsymbol{\kappa}$ is the permeability tensor for each of the four fluid networks; whilst μ defines the viscosity of each fluid. In this work, three of the four fluid domains are isotropic (a, c, v), which implies $\boldsymbol{\kappa} = \kappa\mathbf{I}$, where κ is a constant and **I** is the unit tensor for an isotropic medium. For the CSF/ISF compartment (e), a spatially varying permeability tensor extracted from diffusion-weighted imaging (DWI) was used, as $\boldsymbol{\kappa}$ can be defined in a heterogeneous and anisotropic manner [40].

2.2 NUMERICAL IMPLEMENTATION OF THE MPET SOLVER, VERIFICATION AND MESH INDEPENDENCE

The highly coupled governing equations of the MPET theory have been discretised using the finite element method and implemented into an in-house FORTRAN code. Both the equilibrium equation (the displacement field **u**) and mass conservation equations (scalar pressure p_i), is approximated in the continuous piecewise linear polynomial space. Based on the principle of minimum potential energy, the algebraic form of the equilibrium equation is:

$$\mathbf{K}_s\mathbf{u} - \left(\mathbf{Q}_a\mathbf{p}_a + \mathbf{Q}_c\mathbf{p}_c + \mathbf{Q}_e\mathbf{p}_e + \mathbf{Q}_v\mathbf{p}_v\right) = \mathbf{F} \tag{8}$$

where,

$$\mathbf{K}_s = \int_\Omega \mathbf{B}^T\mathbf{D}\mathbf{B}d\Omega$$

$$\mathbf{Q}_i = \int_\Omega \alpha_i\mathbf{B}^T\mathbf{h}d\Omega$$

$$\mathbf{F} = \int_\Omega N^T\mathbf{b}d\Omega + \int_{\Gamma_N} N^T\mathbf{t}_N d\Gamma$$

$\mathbf{K_s}$ is the stiffness matrix, **B** the deformation matrix and **D** is the elasticity matrix. $\mathbf{Q}_i$ is the load on the solid phase contributed from the ith fluid network and **h** is a mapping vector. **F** is the load vector, **b** is the vector of body forces in the three-dimensional domain Ω, and $\mathbf{t}_N$ the vector of external force at the boundary, Γ_N. The Dirichlet boundary conditions are imposed in a strong way.

For the continuity equations of the fluid networks, the method of weighted residuals and the continuous Galerkin formulation are applied to derive the integral form (weak form) of these mass conservation equations. The continuity equation of the ith fluid network can be written as,

$$\int_\Omega \left[\delta p_i\left(c_i\frac{\partial p_i}{\partial t}\right) + \nabla\delta p_i K_i \nabla p_i - \delta p_i S_{x\to y} - \delta p_i \alpha_i \dot{\varepsilon}\right] d\Omega - \int_{\Gamma_N^i} \nabla\delta p_i q_i d\Gamma = 0 \tag{9}$$

where Γ_N is the boundary where the Neumann boundary condition is applied, and q_i is the flux prescribed in the Neumann boundary condition. The discretised continuity equation of the ith fluid network is:

$$\mathbf{A}\dot{\mathbf{p}} + \mathbf{C}\mathbf{p} = \mathbf{P} \tag{10}$$

where,

$$\mathbf{A} = c_i\int_\Omega \mathbf{N}\mathbf{N}^T d\Omega$$

$$\mathbf{C} = \frac{\kappa_i}{\mu_i}\int_\Omega \nabla\mathbf{N}\nabla\mathbf{N}^T d\Omega \tag{11-13}$$

$$\mathbf{P} = \int_\Omega \left(S_{x\to y}\right)\mathbf{N}d\Omega - \alpha\int_\Omega \dot{\varepsilon}\mathbf{N}d\Omega + \int_{\Gamma_N} q_i\mathbf{N}d\Gamma$$

In the above, **N** is the continuous piecewise linear polynomial functions. The temporal discretisation utilises an implicit backward Euler scheme. The discretised governing equations are solved by the standard preconditioned Krylov subspace (KSP) methods in the Portable, Extensible Toolkit for Scientific Computing (PETSc) library [41-42].

The governing equations of the MPET system have been discretised using the finite element method and implemented into an in-house FORTRAN code, which has been verified [40] against Terzaghi's [43] and Mandel's [44] problems. In addition to the verification, mesh independence (12 meshes with total element numbers ranging from ~100k to ~9 million) of the 3D MPET outputs (displacement, scalar pressures and relevant filtration velocities from the four compartments) using a subject-specific brain geometry has been confirmed [40].

2.3 SUBJECT-SPECIFIC DATASETS

The subject-specific datasets used in the MPET modelling of this paper were collected as part of the VPH-DARE@IT project (www.vph-dare.eu), and prospective data collection was conducted at the Istituto di Ricovero e Cura a Carattere Scientifico (IRCCS) San Camillo, Lido di Venezia, Italy. This study, including a total of 103 people (n = 50 cognitively healthy controls (CHC), age 71.1 ± 7.9 years, and n = 53 with diagnosed MCI, age 75.1 ± 6.7 years), was approved by the joint ethics committee of the Health Authority Venice 12 and the IRCCS San Camillo (Protocol number 2014.08), and all participants gave informed consent prior to participation in the study. A cohort of 35 subjects (n = 20 CHC, n = 15 MCI) was picked from the 103 available subjects. This smaller cohort can be stratified into 4 groups, considering males (M) and females (F): CHC_M (n = 8, age 69.4 ± 8.5 years), CHC_F (n = 12, age 72.5 ± 5.7 years), MCI_M (n = 8, age 75.4 ± 5.0 years) and MCI_F (n = 7, age 74.9 ± 8.2 years).

Each subject had several measurement modalities collected as part of the study, such as: lifestyle questionnaires and neuropsychological tests, whole brain MR imaging, clinical ultrasound flow imaging, portable Holter recordings of blood pressure, and actigraph measured activity levels. Further details can be found in Guo et al. [40]. For the Lido study cohort, Holter recordings and ultrasound flow measurements were used to generate boundary conditions of arterial blood flow using cerebral autoregulation models and lumped parameter circulation models [40, 45], T1-weighted and diffusion-weighted MR images were processed to create accurate 3D whole-brain meshes and finally permeability tensor maps of the parenchyma were extracted using the workflow described in detail in Guo et al. [40].

2.4 SUBJECT-SPECIFIC BOUNDARY CONDITIONS AND PARAMETERS

In Figure 3, the subject-specific modelling pipeline for acquiring personalised cerebral blood flow waveforms [45] that are fed into the arterial compartment of the MPET model [40] is depicted. For each subject, four waveforms were calculated at every time point, which are the ICA blood to the left and right cerebrum (ICA_L and ICA_R), and the vertebral artery (VA) blood to the left and right cerebellum (VA_L and VA_R). In order to apply these subject-specific waveforms as boundary conditions for the arterial compartment in equation 14b, the cortical surface is divided into four perfusion regions corresponding to the four waveforms [40]. Furthermore, the blood flow waveform is of 1 second duration depicting a period of the maximum (high activity) and minimum (low activity) activity during a 24-hour period. Once the Neumann boundary conditions are applied at the partitioned cortical surface, the numerical simulations are executed for 50 cycles (of cerebral blood flow waveforms), for the solution fields to reach a periodic steady state. This approach is adopted in the work of Guo and colleagues [40]. The MPET solutions from the final steady state are used to conduct the statistical analysis.

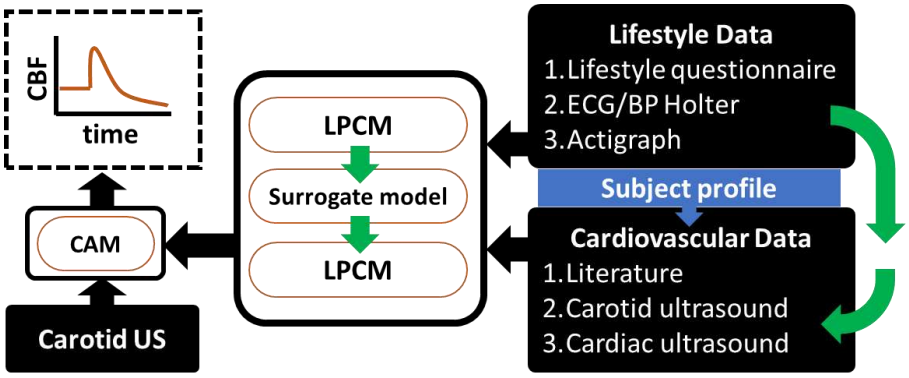

Figure 3. Subject-specific modelling pipeline for acquiring personalised cerebral blood flow waveforms that are fed into the arterial compartment of the MPET model, in the form $\nabla p_a \mathbf{n} = Q_a$. Ageing and lifestyle related patient-specific boundary conditions are generated following the data collection and subject-based model parameterisation. The personalisation of the lumped parameter circulation model (LPCM) was accelerated via a surrogate model to approximate its input-output response [45]. LPCM = Lumped parameter circulation model (based on [46]), CAM = cerebral autoregulation model (based on [47]).

Table 2: Parameters used in the MPET modelling.

Parameters	Values	Units	Parameters	Values	Units
$\alpha_{a,c}$	0.25		$k_{a,c,e,v}$	1.0×10^{-10}	m^2
α_e	0.49		ω_{ac}	1.5×10^{-19}	$m^2N^{-1}s^{-1}$
α_v	0.01		ω_{cv}	1.5×10^{-19}	$m^2N^{-1}s^{-1}$
λ	505	Pa	ω_{ev}	1.0×10^{-13}	$m^2N^{-1}s^{-1}$
G	216	Pa	ω_{ce}	1.0×10^{-20}	$m^2N^{-1}s^{-1}$
L	70×10^{-3}	m	R	8.5×10^{13}	m^{-3}
d	3×10^{-3}	m	Q_p	5.8×10^{-9}	m^3s^{-1}
p_{bp}	650	Pa	Δt	0.1	s
$c_{a,c}$	2.9×10^{-4}	m^2N^{-1}			
c_e	3.9×10^{-4}	m^2N^{-1}			
c_v	1.5×10^{-5}	m^2N^{-1}			

The MPET system is completed with the following boundary conditions for each of the four compartments (a, e, c, v), where $\partial\Gamma_s$ and $\partial\Gamma_v$ are boundaries at the skull and cerebral ventricles respectively, and **n** is the outward unit normal vector.

On the cortical surface:

$$
\begin{aligned}
&\mathbf{u} = \mathbf{0} && \text{on } \partial\Gamma_S,\\
&\text{SSBFP in the form } \nabla p_a \mathbf{n} = Q_a && \text{on } \partial\Gamma_S,\\
&\nabla p_c \mathbf{n}|_{\partial\Gamma_S} = 0 && \text{on } \partial\Gamma_S,\\
&p_v \mathbf{n}|_{\partial\Gamma_S} = p_{bp} && \text{on } \partial\Gamma_S,\\
&p_e|_{\partial\Gamma_S} = p^v|_{\partial\Gamma_S} + \mu^e R Q_o && \text{on } \partial\Gamma_S,\\
&\frac{p_e|_{\partial\Gamma_S} - p_{bp}}{\mu_e R} = \frac{\pi d^4}{128\mu_e L}(p_e|_{\partial\Gamma_V} - p_e|_{\partial\Gamma_S}) + \oint_S (-K_e \cdot \nabla p_e).\mathbf{n}ds && \text{on } \partial\Gamma_S.
\end{aligned}
\tag{14a-f}
$$

On the ventricular wall:

$$
\begin{aligned}
&-p_V \mathbf{n} = \sigma_{ij} \cdot \mathbf{n} && \text{on } \partial\Gamma_V,\\
&\nabla p_a \mathbf{n}|_{\partial\Gamma_V} = 0 && \text{on } \partial\Gamma_V,\\
&-\kappa_{c-vent} \nabla p_c \mathbf{n}|_{\partial\Gamma_V} = Q_p && \text{on } \partial\Gamma_V,\\
&\nabla p_v \mathbf{n}|_{\partial\Gamma_V} = 0 && \text{on } \partial\Gamma_V,\\
&Q_p = \frac{\pi d^4}{128\mu_e L}(p_e|_{\partial\Gamma_V} - p_e|_{\partial\Gamma_S}) - 4\pi k_e\left(r_v + u_1^n\right)\nabla p_e \mathbf{n} + 4\pi\left(r_v + u_1^n\right)^2 \dot{u} && \text{on } \partial\Gamma_V.
\end{aligned}
\tag{15a-e}
$$

Since this is an adult brain that is being taken under consideration; a rigid wall approximation can be envisaged stemming from the elimination of layers like the dura mater and scalp. A subject-specific blood flow profile (SSBFP) depicting a period of high and low activity is used as the BC for the arterial network at the cortical surface.

CSF is assumed to be produced at a constant rate, Q_p within the ventricles. p_{bp} is the blood pressure in the sagittal sinus, $\kappa_{c\rightarrow vent}$ represents the capillary network resistance to the flow from the capillary network, R is the resistance due to the presence of arachnoid granulations and finally Q_o is the efflux of CSF at the region of the skull. r_v represents the radius of the spherical shell encapsulating the cerebroventricular system and u_1 is the maximum ventricular displacement at each time increment. It is necessary to restrict the transfer of water between fluid networks, and Figure 2 depicts a schematic of the setting in which the quadruple MPET model functions. Table 2 gives the complete list of all parameters used to execute the MPET model.

2.5 STATISTICAL ANALYSIS

A Shapiro-Wilk's test ($p > 0.05$ for all cases) is used to assess the normality of the data. Outliers in the ICA and VA based data were assessed by inspection of a boxplot. Levene's test was used to assess for equality of variances, whilst Mauchly's test of sphericity [67] was also used to test the null hypothesis that the variances of the differences of the groups (ICA_R(HA), ICA_L(HA), ICA_R(LA), ICA_L(LA), VA(HA), VA(LA)) considered are equal. A three-way mixed ANOVA was run to understand the effects of gender, cognitive status and activity on blood flow rate in the left and right ICA and VA. All pairwise comparisons were performed for statistically significant simple main effects.

A Kruskal-Wallis H-test [48] was conducted to determine if there were differences in swelling and drainage in the hippocampus of the brain between 4 groups (CHC_M (n = 8), CHC_F (n = 12), MCI_M (n = 8) and MCI_F (n = 7)), during two levels of activity (high and low). Visual inspection of the relevant boxplots was used to determine whether the distributions of swelling and drainage were similar for all groups. This is needed since if the distributions are not similar, one cannot make inferences about differences in medians between groups. Instead, mean ranks are then used for the analysis. Subsequently (where a statistically significant Kruskal-Wallis H-test exists), pairwise comparisons were performed using Dunn's [49] procedure with a Bonferroni correction [50] for multiple comparisons. Adjusted p-values are presented.

A Wilcoxon signed-rank test [51] was used to determine whether there was no statistically significant median decrease in swelling and drainage in the hippocampus when CHC and MCI subjects lowered their activity level. It was assessed whether the differences in swelling and drainage were symmetrically distributed (via a histogram). A Wilcoxon signed-rank test requires the distribution of the differences between the two related groups to be symmetrical in shape. Where this is not the case, a sign test with continuity correction is used, as this test does not make any distributional assumptions.

The statistical analyses were performed using IBM SPSS Statistics, Version 25 (IBM Corp., Armonk, NY).

3. RESULTS

Figure 4 depicts a typical set of results (for one 69-year-old female CHC and one 75-year-old male MCI subject) obtained from running the consolidated pipeline. In the figure, coronal sections of the brain at the level of the hippocampus are depicted. The results pertaining to the NVU fluid content, clearance and perfusion for two subjects, one female CHC and one male MCI, are shown. The intracranial pressure (pore pressure of the CSF/ISF compartment) is also shown, and this solution field was made to overlap with the filtration velocity vectors of the capillary compartment and CSF/ISF compartment respectively. There is a reduction in peak clearance observed between the two subjects, with the female CHC subject having a peak clearance of 24 µm/s compared to 31 µm/s for the male MCI subject. Similar characteristics were observed for swelling and drainage between the two subjects,

with the female CHC possessing lower peak values (1.91 and -0.13) compared to the male MCI subject (1.92 and -0.49). The level of peak perfusion was reversed, with the female CHC possessing higher level of perfusion (0.26 mm/s) compared to the male MCI subject (0.14 mm/s).

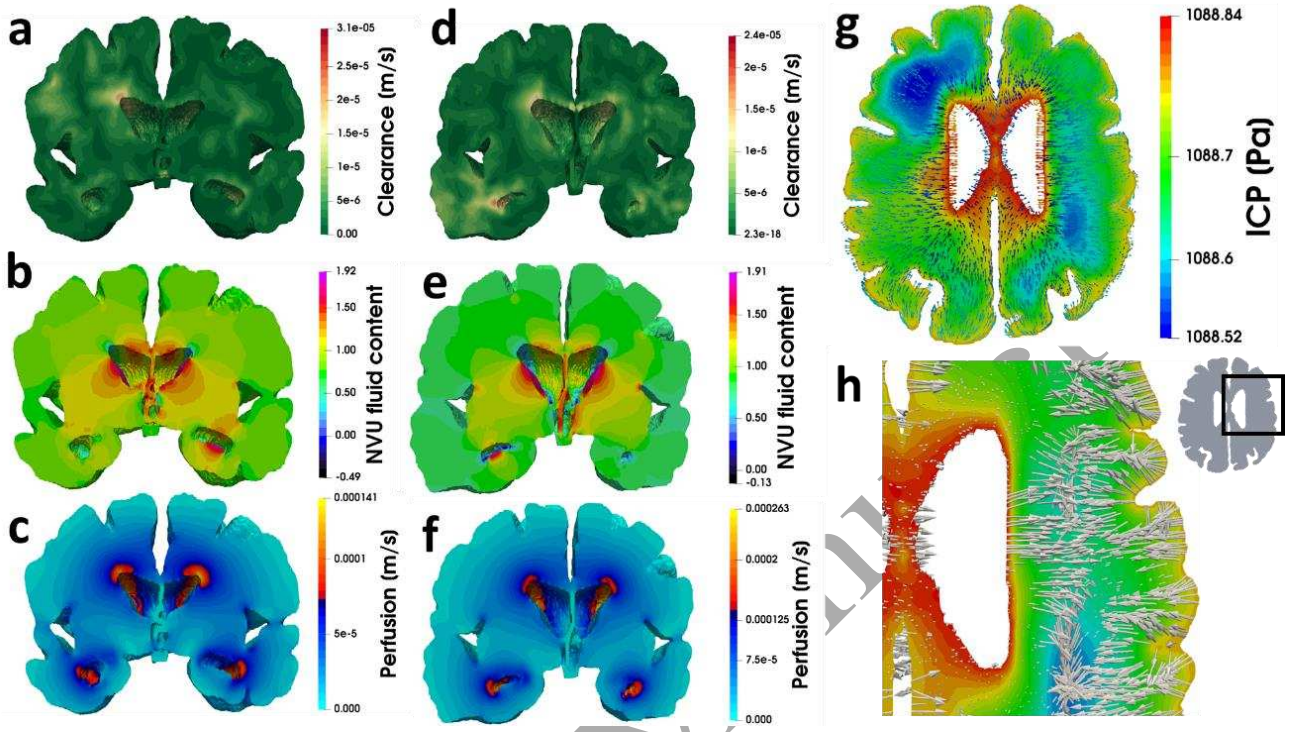

Figure 4. A selection of MPET results for the brain parenchyma. Specifically, clearance (Darcy velocity of the CSF/ISF compartment), perfusion (Darcy velocity of the capillary compartment) and the fluid content of the neurovascular unit (a positive value indicates swelling, and a negative value indicates drainage). (a-c) Coronal section of the brain at the level of the hippocampus for a 75-year-old male MCI subject. (d-f) Coronal section of the brain at the level of the hippocampus for a 69-year-old female CHC subject. (g) An axial slice of the brain (female CHC subject), with the intracranial pressure (pore pressure of the CSF/ISF compartment) solution filed in the parenchyma overlapping the Darcy velocity vectors of the capillary compartment. (h) The intracranial pressure solution field overlapping with the Darcy velocity of the CSF/ISF compartment (female CHC subject). The magnitude of the vectors has been doubled to improve visibility. All results are acquired during a period of high activity.

Blood flow rates in the $ICA_{L/R}$ and VA for males and females (both CHC and MCI) during both high and low activity were normally distributed, as assessed by Shapiro-Wilk's test ($p > 0.05$ for all cases) [68]. There were outliers in the ICA and VA based data for females diagnosed with MCI during the period of low activity, as assessed by inspection of a boxplot. There was homogeneity of variances ($p > 0.05$) for ICA_R(HA), ICA_R(LA), ICA_L(HA), ICA_L(LA), VA(HA) and VA(LA) as assessed by Levene's test. Mauchly's test of sphericity is not violated as there are only two levels of the within-subjects factor (high and low activity) and, therefore, there is only one paired difference. For the right ICA, the three-way interaction between gender, cognitive status and activity was not statistically significant, $F(1, 31) = 0.147$, $p = 0.704$, partial $\eta^2 = 0.005$. Similarly, for the left ICA this was $F(1, 31) = 0.391$, $p = 0.536$, partial $\eta^2 = 0.012$, and for the VA this was $F(1, 31) = 0.267$, $p = 0.609$, partial $\eta^2 = 0.009$. All two-way interactions were not statistically significant ($p > 0.05$). For the four groups considered, the mean CBF and standard deviation of the mean are listed in the following table and approximated to 1 decimal place.

Table 3: Mean CBF and parenchymal tissue volume (with the standard deviation of the mean, SDμ) for the four groups in addition to the overall CHC and MCI cohorts. High activity is indicated by red cells, whilst low activity by the blue cells.

CHC – M + F [ml/min]								**Brain Volume [ml]**
	ICA_L	**ICA_R**	**VA**		**ICA_L**	**ICA_R**	**VA**	
μ	559.7	571.2	141.4		331.0	338.9	83.7	1132.6
SDμ	138.3	120.4	30.6		87.9	72.8	18.7	105.1
CHC - M [ml/min]								
μ	540.6	539.8	135.1		320.8	314.1	79.4	1154
SDμ	164.2	157.0	39.2		103.0	93.0	24.0	144.7
CHC - F [ml/min]								
μ	572.4	592.1	145.6		337.8	355.4	86.7	1117.7
SDμ	116.2	81.5	22.3		75.4	48.8	13.5	62.4
MCI [ml/min] - M + F								
μ	492.5	521.0	126.7		300.4	321.4	77.7	1066.8
SDμ	131.6	115.0	29.5		86.7	70.3	18.2	109.2
MCI - M [ml/min]								
μ	519.1	532.2	131.4		326.2	326.8	81.6	1106.7
SDμ	154.4	112.1	32.0		103.7	62.5	20.0	38.7
MCI - F [ml/min]								
μ	462.1	508.3	121.3		270.8	315.1	73.2	1021.2
SDμ	90.0	117.0	25.2		46.5	77.8	14.7	102.6

As can be seen from Table 3, there peak flow rates that are calculated from the personalised cerebral blood flow waveform pipeline are lower during low activity for the left and right ICA, and VA. It can be observed that grouped (both males and females) CHC subjects possess higher flow rates than the grouped MCI subjects. The stratified results (with respect to gender) indicate that female CHC subjects possessed on average higher flow rates for the left ICA, right ICA, and VA compared to the male CHC cohort, whilst for the MCI subjects, this trend was reversed (MCI males possessed higher flow rates). For all gender specific groups, the flow rates were higher during high activity compared to those recorded during low activity. The parenchymal brain volume (including the cerebral ventricles) for each group is also given in the last column of Table 3, for reference.

A Kruskal-Wallis H-test was conducted to determine if there were differences in swelling and drainage in the hippocampus of the brain between the four (CHC_M, CHC_F, MCI_M and MCI_F) groups, during two levels of activity (high and low). Distributions (see Figure 5) of swelling were not similar for all groups, whilst the distributions of drainage were similar for all groups. Subsequently, a Wilcoxon Signed Rank Test determined whether there was any statistically significant median decrease in swelling and drainage in the hippocampus when subjects of the four groups lowered their activity level. The results for the Kruskal-Wallis H-test is given in Table 4.

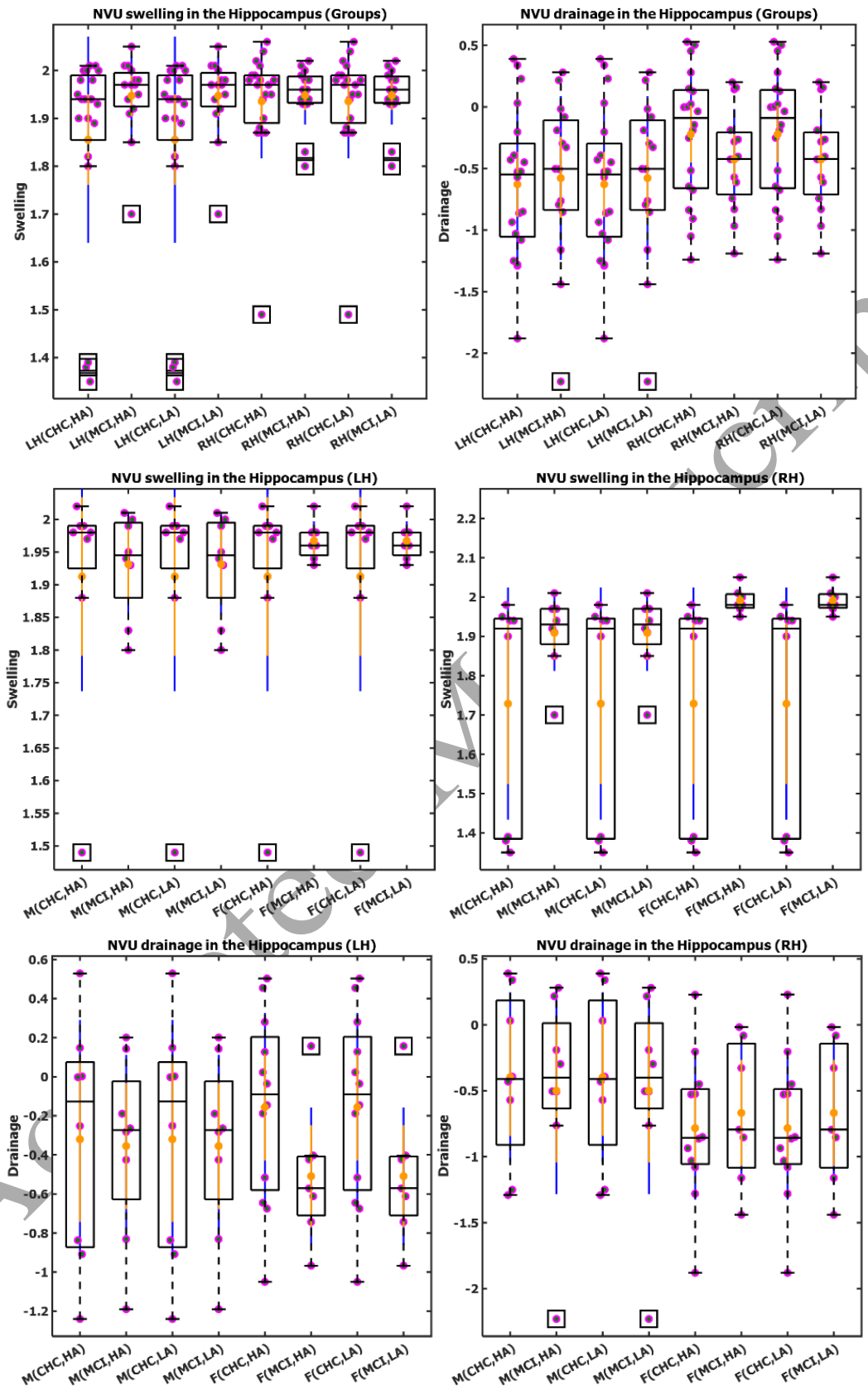

Figure 5. Traditional box and whisker plots (median and 25th,75th percentile) for NVU swelling and drainage (stratified with respect to combined groups (males and females) and individually), with raw data points laid over a 1.96 SEM (95% confidence interval) in orange and a 1 SD in blue. Means are also shown with an orange circle. Raw data are dispersed along the x-direction for clarity. Square black boxes indicate outliers.

Table 4. Kruskal-Wallis H-Test for NVU swelling and drainage in the hippocampus. The test statistic is reported (to an accuracy of two decimal places) as the value of the chi-squared (χ^2) statistic, with 3 degrees of freedom. Distributions of NVU swelling and drainage were not similar for all groups, as assessed by visual inspection of a boxplot. Values are mean ranks unless otherwise stated. Where the Kruskal-Wallis H-test is statistically significant ($p < 0.05$), pairwise comparisons were performed using Dunn's procedure with a Bonferroni correction for multiple comparisons. Adjusted p-values are presented in the post hoc columns. Mean ranks are given in brackets where appropriate. HIPP = Hippocampus, Subscripts: S = swelling, D = drainage, M = male, F = female.

	Right Hemisphere						Left Hemisphere			
	HA			LA			HA		LA	
	χ^2	*p*	post hoc	χ^2	*p*	post hoc	χ^2	*p*	χ^2	*p*
$HIPP_S$	8.929	**0.030**	CHC_M (11.19) and MCI_F (26.36), $p = 0.025$	8.929	**0.030**	CHC_M (11.19) and MCI_F (26.36), $p = 0.025$	0.789	**0.852**	0.789	**0.852**
$HIPP_D$	3.319	**0.345**		3.319	**0.345**		2.369	**0.499**	2.369	**0.499**

In the right hippocampus, the level of NVU swelling was statistically significantly different between the categories of cognitive status and gender during the period of high and low activity, $\chi^2(3) = 8.929$, $p = 0.030$ (for both activity states). Subsequently, pairwise comparisons were performed using Dunn's [49] procedure with a Bonferroni correction for multiple comparisons [50]. The post hoc analysis revealed statistically significant differences in NVU swelling between CHC males (11.19) and MCI females (26.36) ($p = 0.025$) during both activity states, but not between any other group combination. Drainage of the NVU was lower in CHC males (-0.41) than CHC females (-0.86), and higher in MCI females (-0.79) than MCI males (-0.4) during both activity states, but the differences were not statistically significant, $\chi^2(3) = 3.319$, $p = 0.345$ (for both activity states).
In the left hemisphere, there were differences in the degree of swelling and drainage between the four groups, but these were not statistically significant.

When conducting a Wilcoxon Signed Rank Test, it was observed that when comparing the four groups during high and low activity, there were differences in the degree of swelling and drainage, but that these differences were not statistically significant.

4. DISCUSSION

In the work presented here, various advancements have been made in refining the integrity of the qualitative representation of fluid accumulation and drainage and applying it to the level of the BBB. Firstly, the consolidated pipeline has been applied to a cohort of 35 subjects (20 CHC, 15 MCI), and MPET results are statistically analysed at a region-specific level, namely the hippocampus. Secondly, it was hypothesized that physical activity would have an influence in both swelling and drainage.

In Table 1 (specifically, the fluid content relationship), the $c_c p$ term represents the amount of blood (which is also exchanging fluid with the cerebrospinal/interstitial fluid – see Figure 2) that can be injected into a fixed material volume (in this case, the parenchymal tissue), whilst the $\alpha_c \nabla \cdot \mathbf{u}$ term (the Biot-Willis constant, α, is deemed to reflect mechanical compliance [16]) is a measure of the amount of blood that can be squeezed out of the same volume of parenchymal tissue. Importantly, this second term reveals the importance of the scaled (with respect to the Biot-Willis coefficient) strain field within the parenchymal tissue, and the role this plays in determining whether the overall effect of the fluid content is either positive or negative as it is possesses a larger magnitude in the simulations conducted in this work. Of course, this is also dependent on the boundary conditions attributed to pore pressure in the capillary compartment, as in the simulations conducted here, the range in pore pressure was approximately 2.4-2.5 kPa. Enforcing a large pressure on the boundaries would translate into a larger quantity of fluid that can be injected into the fixed parenchymal volume, which would therefore

dampen the influence of the scaled strain, and in the process determining the propensity of the fluid content. It is worth noting that a balance should be struck when determining the optimal course of action here, as being able to account for the influence of the surface concavity (and therefore the accumulation of strain) is beneficial in assessing the macroscopic effects of not only the geometry under consideration (as in the case of the cerebral ventricles), but also the cumulative effect of the imposed boundary conditions on the remaining compartments and the intercompartmental fluxes.

In Figure 5, the effect of incorporating physical activity are negligible. This result at first sight seems unexpected, as the variation in CBF between activity states (see Table 3) that is applied as the arterial boundary conditions to the MPET model (and essentially drives the MPET system) shows a clear reduction during the period of low activity. The value of the constrained specific storage coefficient for the capillary compartment underestimates the contribution of the pore pressure in this compartment and allows the strain field to play a dominant role in determining the resultant fluid content. It is important to note here that the constant strain cross-storage effects relating to the other three compartments are also not incorporated in this formulation, as the usefulness of their inclusion in our model is debatable [52]. An additional limitation is that the current quadruple-MPET model conflates all the fluid outside the vascular tree (CSF and ISF) into a single compartment. This negates the important effects of the paravascular/perivascular spaces, glial cells and the overarching influence of the glymphatic system, which are known to play an important role in BBB breakdown and dysfunction [60,69]. The current MPET model has been recently extended to six compartments (in a simplified, spherically symmetric 1D formulation) and has relaxed the assumption of quasi-steady behaviour [70] in order to account for both aqueductal stenosis during acute hydrocephalus in addition to providing insight into oedema formation [71]. In future work, the 3D extension to this discretization template will be implemented within the consolidated pipeline described in this work.

From figure 4, both swelling and drainage is asymmetric in nature, as the distribution of the results varies between the left and right portion of the hippocampus. The mean swelling in the NVU is higher in the MCI subjects (also considering the stratified results with respect to gender), which can be postulated to signify the higher probability of BBB breakdown or dysregulation within the representative elementary volume of parenchymal tissue that the MPET system covers.

The biomarker defined by the fluid content in the capillary compartment can be deemed to qualitatively describe the physiological cascade of events that evolve due to NVU malfunction in a variety of pathological processes in both acute (such as traumatic brain injury) and chronic conditions (such as AD [53-54]), as these are characterised by an inflammatory response, degradation of the extracellular matrix and loss of permeability and selectivity of the BBB [55]. More specifically, within the brain tissue, BBB breakdown leads to the perivascular accumulation of blood-derived neurotic products which ultimately leads to neuronal injury, cell death and inflammatory response [56], and albumin which contributes to oedema formation (which can be captured by a positive fluid content in the CSF/ISF compartment of the MPET model), hypoperfusion and tissue hypoxia [57]. Detachment, degeneration and loss of pericytes (see figure 2) also leads to BBB breakdown [58]. As opposed to BBB breakdown, a dysregulated BBB effects the key mechanisms behind Aβ homeostasis in the brain [59] and can lead to inefficient drainage along the perivascular route which is signified by Aβ accumulating in the space between the astrocytic end-feet and the blood vessel walls (perivascular space – see figure 2) [60]. It has been noted in previous work by the same authors that when considering the CSF/ISF compartment, the fluid content was here used to describe periventricular lucency, and in doing so, conceptual links could be made with the swelling activated components of the parenchymal tissue microstructure [40,61].

There is evidence to suggest that a disruption to the BBB compromises Aβ clearance at the level of the NVU, which is postulated to result in a cycle between Aβ accumulation and BBB dysfunction during AD progression [62]. Aβ has been deemed a likely candidate in the disruption of tight junctions in endothelial cells, which ultimately perturbs the ability of the endothelial cells to function as an effective barrier. In the results presented for NVU swelling in the hippocampus, the mean swelling in

the left and right portions of the hippocampus are lower for CHC subjects when compared to MCI subjects (1.94 and 1.86 compared to 1.95 and 1.95). The level of drainage in the NVU is asymmetric between the two sets of subjects, as the left hippocampal portion portrayed more pronounced mean drainage (-0.22 for CHCs compared to -0.42 for MCIs) compared to the right portion (-0.63 for CHCs compared to -0.58 for MCIs). When stratifying the results with respect to gender, male and female CHC subjects displayed lower degrees of swelling and drainage in both hippocampal portions compared to male and female MCI subjects. Further analysis revealed statistically significant differences in NVU swelling between CHC males (11.19) and MCI females (26.36) ($p = 0.025$) during both activity states for the right hemisphere.

5. CONCLUSIONS

This paper describes a three-dimensional multicompartmental poroelasticity model for perfused parenchymal tissue coupled with an automated image-based model personalization workflow, and a subject-specific blood flow variability model. This unified pipeline is used on a cohort of 35 subjects (stratified with respect to gender and disease status) to provide insight (statistically analysis) into the underlying mechanisms of the neurovascular unit (NVU) in the hippocampal region of the brain, and to ascertain whether physical activity would have an influence in both swelling and drainage by taking into account the scaled strain field and the proportion of perfused blood injected into the brain tissue. A key result garnered from his study is the statistically significant differences in hippocampal (the right portion) NVU swelling between CHC males and MCI females during both activity states.

In future work, revised estimates for the constrained specific storage coefficients need to be established, as these allow for the percolation of fluid between networks to be more accurately captured. It has been postulated that systemic hypertension causes stiffening and microvascular distortion of vessels, increased tortuosity and thickened membranes in arterioles, and is associated with a reduction of capillary density [63]. The CSF/ISF and capillary compartments can be used to link microvascular permeability and overall cerebral compliance, and therefore provide further insight (via rule-based remodelling processes which will also need to account for white matter changes associated with AD [65]) into the influence of lifestyle and environmental factors of interest and the extent of chronic cerebral hypoperfusion (promoting the notion of age-dependent vascular compliance [66]). Finally, tortuosity may be better served by more intricate models (as opposed to Darcy's law) of flow in porous media (such as the Blake-Kozeny-Carman (BKC) model [64] for a packed bed).

ETHICS

This prospective data collection was approved by the joint ethics committee of the Health Authority Venice 12 and the IRCCS San Camillo (Protocol number 2014.08), and all participants gave informed consent prior to participation in the study.

COMPETING INTERESTS

We declare we have no competing interests.

FUNDING

The work has been supported by the European Commission FP7 project VPH-DARE@IT (FP7-ICT-2011-9-601055), and partially by the EPSRC-funded projects OCEAN (EP/M006328/1) and EPSRC-NIHR HTC Partnership Award 'Plus': Medical Image Analysis Network (EP/N026993/1).

ACKNOWLEDGEMENTS

We want to thank Dr J. Willems and Dr M. Megahed from the ESI Group for the valuable discussions regarding the verification of the 3D MPET model.

REFERENCES

[1] Dowell, E. H. and K. C. Hall (2001). Modeling of Fluid-Structure Interaction. Annual Review of Fluid Mechanics 33(1): 445-490.
[2] Biot MA. (1941). General theory of three-dimensional consolidation. J. Appl. Phys. 12, 155–164.
[3] Biot, MA. (1955). Theory of elasticity and consolidation for a porous anisotropic media. J. Appl. Phys. 26(2), 182–185
[4] Terzaghi, K. (1925). Principle of soil mechanics. Eng. News Record, A Series of Articles
[5] Phillips, P.J. & Wheeler, M.F. (2008). A coupling of mixed and discontinuous Galerkin finite-element methods for poroelasticity. Comput Geosci 12(4), 417-435
[6] Barenblatt, G. I., Zheltov, I. P. & Kochina, I. N. 1960. Basic concepts in the theory of seepage of homogeneous liquids in fissured rocks [strata]. Journal of Applied Mathematics and Mechanics, 24, 1286-1303.
[7] Di Luca, M., Nutt, D., Oertel, W., Boyer, P., Jaarsma, J., Destrebecq, F., Esposito, G., Quoidbach, V. (2018). Towards earlier diagnosis and treatment of disorders of the brain. Bulletin of the World Health Organization, 96(5), 298-298A.
[8] Cermakova P, Eriksdotter M, Lund LH, Winblad B, Religa P, Religa D. (2015). Heart failure and Alzheimer′s disease (Review). J Intern Med; 277: 406–425.
[9] Wallin K, Bostrom G, Kivipelto M, Gustafson Y. (2013). Risk factors for incident dementia in the very old. Int Psychogeriatr; 25: 1135–43.
[10] Kivipelto M, Helkala EL, Laakso MP et al. (2001). Midlife vascular risk factors and Alzheimer's disease in later life: longitudinal, population based study. BMJ; 322: 1447–51.
[11] Kivipelto M, Ngandu T, Fratiglioni L et al. (2005). Obesity and vascular risk factors at midlife and the risk of dementia and Alzheimer disease. Arch Neurol; 62: 1556–60.
[12] Huang W, Qiu C, von Strauss E, Winblad B, Fratiglioni L. (2004). APOE genotype, family history of dementia, and Alzheimer disease risk: a 6-year follow-up study. Arch Neurol; 61: 1930–4.
[13] Qiu C, Winblad B, Marengoni A, Klarin I, Fastbom J, Fratiglioni L. (2006). Heart failure and risk of dementia and Alzheimer disease: a population-based cohort study. Arch Intern Med; 166: 1003–8.
[14] Gorelick, P. B., Furie, K. L., Iadecola, C., Smith, E. E., Waddy, S. P., Lloyd-Jones, D. M., Bae, H. J., Bauman, M. A., Dichgans, M., Duncan, P. W., Girgus, M., Howard, V. J., Lazar, R. M., Seshadri, S., Testai, F. D., van Gaal, S., Yaffe, K., Wasiak, H., Zerna, C. (2017). American Heart Association/American Stroke Association. Defining Optimal Brain Health in Adults: A Presidential Advisory From the American Heart Association/American Stroke Association. Stroke, 48(10), e284-e303.
[15] Brookmeyer R, Johnson E, Ziegler-Graham K, Arrighi HM. (2007). Forecasting the global burden of Alzheimer's disease. Alzheimers Dement; 3: 186–91.
[16] Tully B, Ventikos Y. (2011). Cerebral water transport using multiple-network poroelastic theory: application to normal pressure hydrocephalus. Journal of Fluid Mechanics 667: 188-215.
[17] Rekate HL. (2009). A contemporary definition and classification of hydrocephalus. Semin Pediatr Neurol 16: 9-15.
[18] Thompson D. (2009). Hydrocephalus. Neurosurgery 27: 130-134.
[19] Stagno V, Navarette EA, Mirone G, Esposito F. (2012). Management of Hydrocephalus Around the World. World Neurosurgery.
[20] Vardakis JC, Tully BJ, Ventikos Y. (2013). Multicompartmental Poroelasticity as a Platform for the Integrative Modeling of Water Transport in the Brain. In: Holzapfel GA, Kuhl E, editors. Computer Models in Biomechanics: Springer Netherlands. pp. 305-316.
[21] Corns R, Martin A. (2012). Hydrocephalus. Neurosurgery 30: 142-148.
[22] Kartal, M. G., & Algin, O. (2014). Evaluation of hydrocephalus and other cerebrospinal fluid disorders with MRI: An update. Insights into imaging, 5(4), 531-41.
[23] Tarasoff-Conway JM et al. (2015). Clearance systems in the brain—implications for Alzheimer disease. Nat. Rev. Neurol. 11, 457–470.
[24] Ramanathan A, Nelson AR, Sagare AP, Zlokovic BV. (2015). Impaired vascular-mediated clearance of brain amyloid beta in Alzheimer's disease: the role, regulation and restoration of LRP1. Front. Aging Neurosci. 7, 136.
[25] Gottesman RF et al. (2017). Association between midlife vascular risk factors and estimated brain amyloid deposition. JAMA 317, 1443–1450.
[26] Roher AE et al. (2012). Cerebral blood flow in Alzheimer’s disease. Vasc. Health Risk Manag. 8, 599–611.

[27] Thomas T, Miners S, Love S. (2015) Post-mortem assessment of hypoperfusion of cerebral cortex in Alzheimer's disease and vascular dementia. Brain 138, 1059–1069.
[28] de la Torre JC. (2004) Is Alzheimer's disease a neurodegenerative or a vascular disorder? Data, dogma, and dialectics. Lancet Neurol. 3, 184–190
[29] Drachman DA. (2014). The amyloid hypothesis, time to move on: amyloid is the downstream result, not cause, of Alzheimer's disease. Alzheimer's Dement. 10, 372–380.
[30] Austin BP, Nair VA, Meier TB, Xu G, Rowley HA, Carlsson CM, Johnson SC, Prabhakaran V. (2011). Effects of hypoperfusion in Alzheimer's disease. J. Alzheimer's Dis. 26(Suppl. 3), 123–133.
[31] Thomas T, Miners S, Love S. (2015). Post-mortem assessment of hypoperfusion of cerebral cortex in Alzheimer's disease and vascular dementia. Brain 138, 1059–1069.
[32] Mazza M, Marano G, Traversi G, Bria P, Mazza S. (2011). Primary cerebral blood flow deficiency and Alzheimer's disease: shadows and lights. J Alzheimers Dis; 23: 375–89.
[33] Ruitenberg A, den Heijer T, Bakker SL et al. (2005). Cerebral hypoperfusion and clinical onset of dementia: the Rotterdam Study. Ann Neurol; 57: 789–94.
[34] Iadecola, C. (2004). Neurovascular regulation in the normal brain and in Alzheimer's disease. Nature Reviews Neuroscience 5: 347-360.
[35] Thal, D. R., Griffin, W. S. T., de Vos, R. A. I., & Ghebremedhin, E. (2008). Cerebral amyloid angiopathy and its relationship to Alzheimer's disease. Acta Neuropathologica, 115(6), 599-609.
[36] Greenberg SM, Gurol ME, Rosand J, Smith EE. (2004). Amyloid angiopathy-related vascular cognitive impairment. Stroke; 35: 2616–9.
[37] Okamoto Y, Yamamoto T, Kalaria RN et al. (2012). Cerebral hypoperfusion accelerates cerebral amyloid angiopathy and promotes cortical microinfarcts. Acta Neuropathol; 123: 381–94.
[38] Bondi, M., Edmonds, E., & Salmon, D. (2017). Alzheimer's Disease: Past, Present, and Future. Journal of the International Neuropsychological Society, 23(9-10), 818-831.
[39] Halliday, G. (2017). Pathology and hippocampal atrophy in Alzheimer's disease. The Lancet Neurology, 16(11), 862-864.
[40] Guo, L., Vardakis, J. C., Lassila, T., Mitolo, M., et al. (2018). Subject-specific multi-poroelastic model for exploring the risk factors associated with the early stages of Alzheimer's disease. Interface Focus, 8(1).
[41] Balay, S., Abhyankar, S., Adams, M. F., et al. (2018a). PETSc Web page http://www.mcs.anl.gov/petsc.
[42] Balay, S., Abhyankar, S., Adams, M. F., et al. (2018b). PETSc Users Manual, ANL-95/11 - Revision 3.9. Argonne National Laboratory.
[43] Terzaghi K. (1925). Erdbaumechanik auf bodenphysikalischer grundlage. Vienna, Austria: F. Duticke.
[44] Mandel J. (1953). Consolidation des sols (étude mathématique). Géotechnique 30, 287–289.
[45] Lassila, T., Marco, L. Y. D., Mitolo, M., Iaia, V., Levedianos, G., Venneri, A., & Frangi, A. F. (2018). Screening for Cognitive Impairment by Model-Assisted Cerebral Blood Flow Estimation. IEEE Transactions on Biomedical Engineering, 65(7), 1654-1661.
[46] M. Ursino. (1998). Interaction between carotid baroregulation and the pulsating heart: A mathematical model, Amer. J. Physiol., vol. 275, no. 5, pp. H1733-H1747.
[47] Mader, G., Olufsen, M., & Mahdi, A. (2015). Modeling Cerebral Blood Flow Velocity During Orthostatic Stress. Annals of Biomedical Engineering, 43(8), 1748-1758.
[48] Kruskal, W. H., & Wallis, W. A. (1952). Use of ranks in one-criterion variance analysis. Journal of the American Statistical Association, 47(260), 583-621.
[49] Dunn, O. J. (1964). Multiple comparisons using rank sums. Technometrics, 6, 241-252.
[50] Armstrong, R. A. (2014). When to use the Bonferroni correction. Ophthalmic and Physiological Optics, 34(5), 502-508. doi: doi:10.1111/opo.12131
[51] Gibbons, J. D., and S. Chakraborti. Nonparametric Statistical Inference, 5th Ed., Boca Raton, FL: Chapman & Hall/CRC Press, Taylor & Francis Group, 2011.
[52] Vardakis, J. C., Chou, D., Guo, L., Tully, B. J., & Ventikos, Y. (2017). Response to letter to the editor concerning "A fully dynamic multi-compartmental poroelastic system: Application to aqueductal stenosis". J Biomech, 58, 243-246.
[53] Busch, S., Wu, L., Feng, Y., Gretz, N., Hoffmann, S., & Hammes, H. P. (2012). Alzheimer's disease and retinal neurodegeneration share a consistent stress response of the neurovascular unit. Cell Physiol Biochem, 30(6), 1436-1443.
[54] Sagare, A. P., Bell, R. D., & Zlokovic, B. V. (2012). Neurovascular dysfunction and faulty amyloid beta-peptide clearance in Alzheimer disease. Cold Spring Harb Perspect Med, 2(10). doi: 10.1101/cshperspect.a011452

[55] Muoio, V., Persson, P. B., & Sendeski, M. M. (2014). The neurovascular unit - concept review. Acta Physiol (Oxf), 210(4), 790-798.
[56] de Vries, H. E., Kooij, G., Frenkel, D., Georgopoulos, S., Monsonego, A., & Janigro, D. (2012). Inflammatory events at blood-brain barrier in neuroinflammatory and neurodegenerative disorders: implications for clinical disease. Epilepsia, 53 Suppl 6(Suppl 6), 45-52.
[57] Yang, Y., & Rosenberg, G. A. (2011). Blood-brain barrier breakdown in acute and chronic cerebrovascular disease. Stroke, 42(11), 3323-8.
[58] Montagne, A., Zhao, Z., & Zlokovic, B. V. (2017). Alzheimer's disease: A matter of blood–brain barrier dysfunction? The Journal of Experimental Medicine, 214(11), 3151-3169.
[59] Koizumi, K., Wang, G., & Park, L. (2015). Endothelial Dysfunction and Amyloid-β-Induced Neurovascular Alterations. Cellular and molecular neurobiology, 36(2), 155-65.
[60] Iliff, J. J., Wang, M., Liao, Y., Plogg, B. A., et al. (2012). A paravascular pathway facilitates CSF flow through the brain parenchyma and the clearance of interstitial solutes, including amyloid β. Science translational medicine, 4(147).
[61] Vardakis, J. C., Chou, D., Tully, B. J., Hung, C. C., Lee, T. H., Tsui, P.-H., & Ventikos, Y. (2016). Investigating cerebral oedema using poroelasticity. Medical Engineering and Physics, 38(1), 48-57.
[62] Yamazaki, Y., & Kanekiyo, T. (2017). Blood-Brain Barrier Dysfunction and the Pathogenesis of Alzheimer's Disease. Int J Mol Sci, 18(9). doi: 10.3390/ijms18091965
[63] Iadecola, C. (2013). The pathobiology of vascular dementia. Neuron, 80(4), 844-866.
[64] Sochi, T. (2010). Non-Newtonian flow in porous media. Polymer, 51, 5007-5023.
[65] Amlien IK, Fjell AM. (2014). Diffusion tensor imaging of white matter degeneration in Alzheimer's disease and mild cognitive impairment. Neuroscience. 276,206-15.
[66] Tanaka, H., Dinenno, F. A., Monahan, K. D., Clevenger, C. M., DeSouza, C. A., & Seals, D. R. (2000). Aging, habitual exercise, and dynamic arterial compliance. Circulation, 102(11), 1270-1275.
[67] Mauchly, J. W. (1940). Significance Test for Sphericity of a Normal n-Variate Distribution. The Annals of Mathematical Statistics. Vol. 11, 204–209.
[68] Shapiro S.S., & Wilk, M.B. (1965). An analysis of variance test for normality (complete samples), Biometrika, 52(3-4), 591–611.
[69] Sweeney, M.D., Zhao, Z., Montagne, A., Nelson, A.R., Zlokovic, B.V. (2018). Blood-Brain Barrier: From Physiology to Disease and Back. Physiol Rev, 99, 21-78.
[70] Chou, D., Vardakis, J.C., Guo, L., Tully, B.J., Ventikos, Y. (2016). A fully dynamic multi-compartmental poroelastic system: Application to aqueductal stenosis. Journal of Biomechanics, 49, 2306-2312.
[71] Chou, D. (2016). Computational modelling of brain transport phenomena: application of multicompartmental poroelasticity (PhD thesis). University of Oxford.
[72] Vardakis, J.C., Tully, B.J., Ventikos, Y. (2013). Exploring the Efficacy of Endoscopic Ventriculostomy for Hydrocephalus Treatment via a Multicompartmental Poroelastic Model of CSF Transport: A Computational Perspective. PLoS ONE, 8 (12).
[73] Kaczmarek, M., Subramaniam, R., Neff, S. (1997). The hydromechanics of hydrocephalus: steady-state solutions for cylindrical geometry. Bull. Math. Biol., 59, 295-323
[74] Levine, D.N. (1999). The Pathogenesis of Normal Pressure Hydrocephalus: A Theoretical Analysis. Bull. Math. Bio., 61, 875-916.
[75] Levine, D.N. (2000). Ventricular size in pseudotumor cerebri and the theory of impaired CSF absorption. J. Neurolog. Sci., 177 (2), 85-94.
[76] Smillie, A., Sobey, I., Molnar, Z. (2005). A hydroelastic model of hydrocephalus. J. Fluid Mech., 539, 417-443.
[77] Sobey, I., Wirth, B. (2006). Effect of non-linear permeability in a spherically symmetric model of hydrocephalus. Math. Med. Biol., 23, 339-361.
[78] Shahim, K., Drezet, J.M., Martin, B.A., Momjian, S. (2012). Ventricle equilibrium position in healthy and normal pressure hydrocephalus brains using an analytical model. J. Biomech. Eng., 134 (4).
[79] Aldea, R., Weller, R.O., Wilcock, D.M., Carare, R.O., Richardson, G. (2019). Cerebrovascular Smooth Muscle Cells as the Drivers of Intramural Periarterial Drainage of the Brain.
[80] Thompson, T.B., Riviere, B.M., Knepley, M.G. (2019). An implicit discontinuous Galerkin method for modeling acute edema and resuscitation in the small intestine. Mathematical Medicine and Biology: A Journal of the IMA.